Development and Analysis of a Long-Stroke Spring Guiding System

Kuang-Yuh Huang
Associate Professor
e-mail: kyhuang@ntu.edu.tw

Chi-hwa Ho

Department of Mechanical Engineering,
National Taiwan University,
1, Sec. 4, Roosevelt Road,
Taipei,
Taiwan 10764, ROC

Inspired by the operating principle of a tank's track, we have developed a long-stroke spring guiding system with belt-shaped springs. Other than those characteristics of normal spring guides, the long-stroke spring guiding system has longer guided stroke and adjustable recovery force. To study the mechanical characteristics of the system, experiments and analyses are carried out. The finite element analysis software ABAQUS is applied to analyze the stress and the recovery force of the preloaded spring guiding during the guiding process, and the Buckingham pi theorem is utilized to investigate the complicated relationships among the geometric parameters, the working parameters, and the guiding properties. According to the analytical and experimental results, an efficient design process and design criteria for the guiding system are concluded and practically validated. Moreover, the system can be easily scaled down or modified to adapt to the applications in precision systems and microsystems due to its simple form and great variability.
[DOI: 10.1115/1.1803853]

1 Introduction

A linear actuator can move precisely with assistance of a guiding system in a well-defined track. However, the conventional guiding system always has to compromise between guiding gaps and friction forces, which induce either guiding errors or decrease positioning resolutions. In contrast, a spring guiding system defines guiding function through elastic properties of material, which is one of the guiding principles for precision machines [1]. This system has some advantages over those conventional ones in the following aspects: no guiding gap, frictionless, no wear, no complicated parts, no maintenance needed, etc. Moreover, the spring can realize not only linear and rotational guiding movement, but also yields the guided part the recovery force to cancel out all possible gaps. Spring guides are widely applied in precision applications such as microvalves [2], microrobots [3,4], micromirrors [5], high stiffness precision actuators [6], optical pickup actuators [7], and scanning actuators for scanning tunnel microscopes [8]. Normally, the guided stroke is limited by the geometric form and the boundary constraint. The monolithic flexure device used in micropositioners has a guided stroke of about 1/100 spring size, and some others with special forms can even reach a stroke up to 1/10 spring size [9–12]. Besides those microspring guides being developed, a long-stroke guiding system with electroformed tracks for linear positioning of space camera has also been registered in a German patent [13]. Based on the principle of a tank's track, we develop a long-stroke spring guiding system with steel spring sheets. The structure of the system can be easily scaled down or modified due to its simple form and great variability, and which allows wide applications in precision systems and microsystems. Additionally, alternatives of spring materials can vary from passive to active. By applying active materials such as shape memory alloys, the currently developed guiding system is able to integrate the guiding and the actuating functions compactly.

The spring guide, being made of an elastically bent and preloaded spring sheet, has a belt shape. During the guiding process, the belt-shaped spring deforms and flattens through rolling and which results in mechanical energy exchange. And along the long axis, the spring has the maximum deformation and stress. To keep a reversible energy transformation, the spring must always operate under elastic deformation conditions. The finite element analysis software ABAQUS is applied to analyze the stress and the force of the preloaded and rolling spring, and the Buckingham pi theorem is employed to investigate the relationships among the maximum stress, the preload forces, the preload stiffness, the recovery forces, and the axial stiffness. According to these relationships and definite boundary conditions deduced, we derive some useful design criteria for the long-stroke spring guiding system. We also build up a theoretical model with equivalent springs to analyze the guiding error induced by this balance change. Furthermore, we apply the finite element method (FEM) analysis to study the lateral stiffness of the spring guide and then develop improving approaches for the system. The performance of spring guide developed here is validated by experimental testing and shown to be in accordance with our design concept.

2 Stress and Strain Analysis

The basic construction of our currently designed long-stroke spring guiding system is shown in Fig. 1, which consists of an elastically preloaded belt-shaped spring sheet. The belt-shaped spring is installed between the mover and the base plate and it makes rolling movement to guide the mover to move linearly. Besides, the belt-shaped spring also provides the recovery force for the mover.

A flat spring sheet is elastically bent and preloaded to achieve the belt shape. The stress distribution of the guiding system and its performance can be affected by the initial bending and preloading condition. To keep a reversible elastic energy transformation, the maximum stress of the preloaded belt-shaped spring must be kept smaller than the yield strength during the guiding process. Being symmetrical in form, the belt-shaped spring is simplified by a theoretical model with a half round spring.

Under a preload force, the belt-shaped spring is partially deformed into an elliptical form. Figure 2 shows the relations between the preload displacement δ and the geometric parameters prior to and after preload applied. Before the spring is preloaded, the length of the half belt-shaped spring $l=\pi\cdot r_0$. The preload displacement δ makes the spring deform from half round into half elliptical, and the change of its perimeter l can be described by Eq. (1):

$$l=2x_1+\frac{\pi}{2}\left[\frac{3}{2}(a+b)-\sqrt{ab}\right], \tag{1}$$

Contributed by the Mechanisms and Robotics Committee for publication in the JOURNAL OF MECHANICAL DESIGN. Manuscript received April 3, 2003; revised March 17, 2004. Associate Editor: C. Mavroidis.

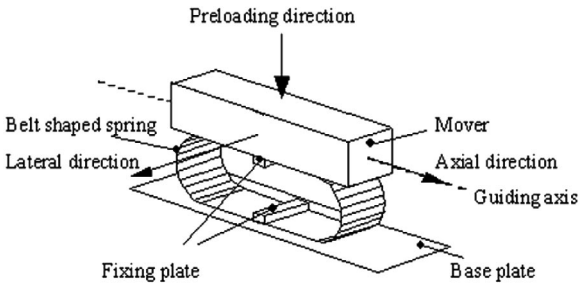

Fig. 1 Basic construction of linear guiding system with a belt-shaped spring

where X_1 is the contact length between the spring and the base plate, a and b are the major axis and the minor axis of the elliptical spring, respectively.

The minor axis b can be expressed by

$$b = r_0 - \frac{\delta}{2}. \tag{2}$$

For the purpose of universal analyses, Eq. (1) being divided by the initial radius r_0 is transformed into the following formula:

$$\frac{l}{r_0} = 2\frac{x_1}{r_0} + \frac{\pi}{2}\left[\frac{3}{2}\left(\frac{a}{r_0} + \frac{b}{r_0}\right) - \sqrt{\frac{a}{r_0}\frac{b}{r_0}}\right]. \tag{3}$$

By using the dimensionless parameters $n = x_1/r_0$, $m = \delta/r_0$, and $p = a/r_0$, Eq. (3) is transformed into Eq. (4):

$$n = \frac{\pi}{8} - \frac{3\pi}{8}p + \frac{3\pi}{16}m + \frac{\pi}{4}\sqrt{p\cdot\left(1 - \frac{1}{2}m\right)}. \tag{4}$$

By squaring Eq. (4), the relation between the geometric parameters (p and n) and the preload displacement ratio m can be derived:

$$p = \frac{-O \pm \sqrt{O^2 - 4\left(\frac{3\pi}{8}\right)^2\left(n - \frac{\pi}{8} - \frac{3\pi}{16}m\right)^2}}{2\left(\frac{3\pi}{8}\right)}, \tag{5}$$

where

$$O = 2\left(\frac{3\pi}{8}\right)\left(n - \frac{\pi}{8} - \frac{3\pi}{16}m\right) - \frac{\pi^2}{16}\left(1 - \frac{1}{2}m\right).$$

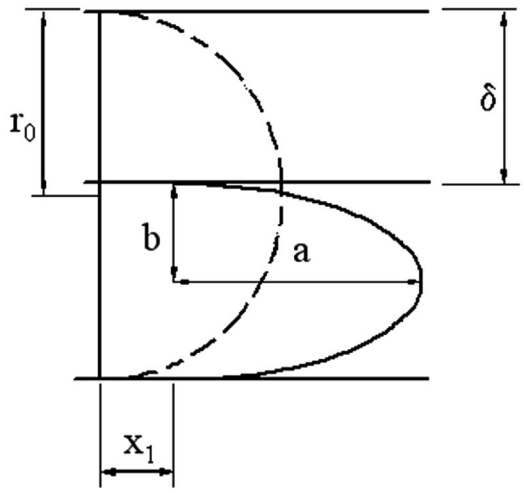

Fig. 2 Half belt-shaped spring prior to and after preload

By means of the curve fitting of the solutions from Eq. (5), the relation between the geometric parameter p and the preload parameter m can be defined as the dimensionless shape equation:

$$p = 0.1811m^3 - 0.7144m^2 + 0.2173m + 1.011, \tag{6}$$

and the relation between the geometric parameter n and the preload parameter m can be given as

$$n = -0.1851m^3 + 0.6752m^2 + 0.1416m - 0.0014. \tag{7}$$

Based on the assumption of an elliptical form ($x^2/a^2 + y^2/b^2 = 1$), the radius of curvature ρ on the preload spring can be expressed by

$$\rho = \left|\frac{[1 + (dy/dx)^2]^{3/2}}{d^2y/dx^2}\right| = \left|\frac{(a^4y^2 + b^4x^2)^{3/2}}{a^4b^2y^2 + a^2b^4x^2}\right|. \tag{8}$$

The maximum stress of the elastically bent spring appears on the major axis a with the radius of curvature $\rho = b^2/a$, and from which the dimensionless curvature parameter w can be derived,

$$w = \frac{\rho}{r_0} = \frac{(b/r_0)^2}{a/r_0} = \frac{(1 - m/2)^2}{p}, \tag{9}$$

and through the shape equations and the material properties of the spring, the maximum stress and the allowed deformation are derived. The maximum stress σ of the half elliptical spring is expressed:

$$G = \frac{\sigma}{E_m} = \frac{c}{\frac{\rho}{r_0}\times\frac{r_0}{I^{1/4}}} = \frac{0.23}{w\times H}, \tag{10}$$

where E_m is the Young's modulus of the spring, H is the dimensionless deformation parameter for the ratio of the initial radius r_0 to the moment of inertia $I^{1/4}$, and the constant c is derived from the experimental stress data of the spring applied.

From Eqs. (6) and (9), the maximum stress parameter G can be expressed by

$$G = \frac{c}{w\cdot H} = \frac{c\cdot(0.1811m^3 - 0.7144m^2 + 0.2173m + 1.0111)}{H\cdot(1 - 0.5m)^2}. \tag{11}$$

The analytical results derived from Eq. (11) are very close to that from the FEM. For analyzing the belt-shaped spring with variable cross sections, the FE method is, in comparison with the other current analytical methods, more flexible in transforming the design data of spring into the FE analytical model. The finite element analysis software ABAQUS was applied to analyze the stress and strain distribution and the recovery force. A 39.28 $\times$12.70$\times$0.05-mm (L$\times$W$\times$T) DIN Ck101 carbon steel sheet was applied to experiments and analyses. The shell element S4R was chosen to model the spring, because it can allow more variation of spring's thickness. And the rigid element R3D4 was used for modeling the guided surface and the base plate, which deliver a contact boundary for the spring. For one-dimensional guided movement, the belt-shaped spring was longitudinally modeled by 20$\times$1 linear elements S4R; and for the lateral displacement, the spring was totally modeled by 20$\times$8 elements. Figure 3 shows the stress distributions of a preloaded belt-shaped spring by the preload displacements of 8.83 mm (curve A) and 15.83 mm (curve B). The maximum stress of curve B nearly reaches the yield strength of 1400 N/mm^2.

The maximum stress σ_{max} of the preloaded spring is associated with four parameters which are (i) the initial radius r_0 of the spring before preloading, (ii) the preload force F_{pre} or preload displacement δ, (iii) the Young's modulus E of the spring material, and (iv) the moment of inertia I of the spring. By applying the Buckingham pi theorem [14,15], these five parameters, σ_{max}, F_{pre}, r_0, E, and I, are collectively transformed into the follow-

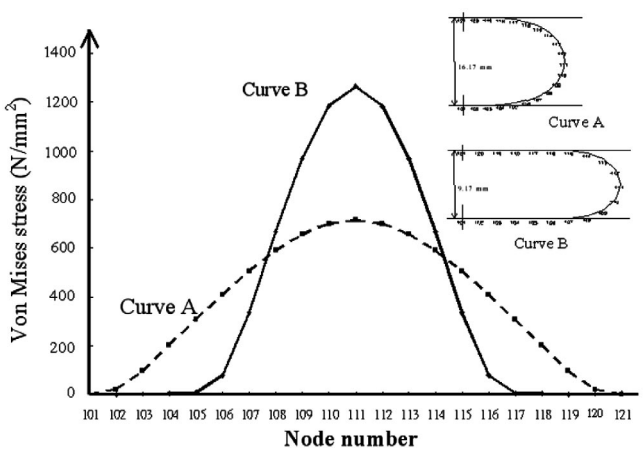

Fig. 3 Stress distributions of a preloaded half belt-shaped spring for two preload situations

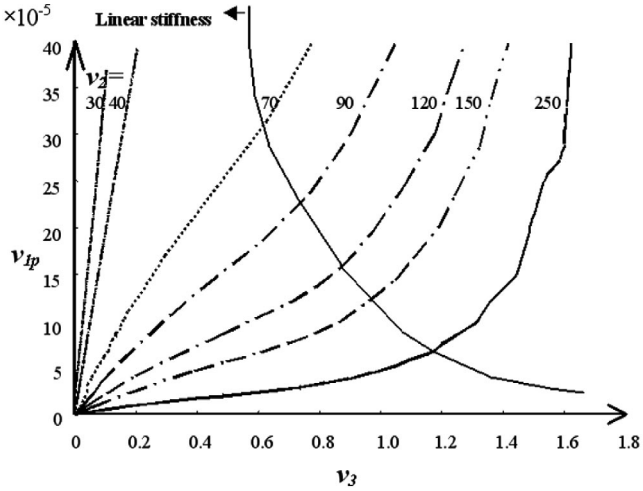

Fig. 5 Preload force ratio v_{1p} versus preload displacement ratio v_3 for different initial radius ratios v_2 ($v_{1p}-v_3$ curves)

ing dimensionless Eq. (12) to ascertain the relationships among the maximum stress, the preload force, and the initial radius:

$$S=\frac{\sigma_{\max}}{E}=f\left(\frac{F_{\text{pre}}}{EI^{1/2}},\frac{r_0}{I^{1/4}}\right)=f(v_{1p},v_2), \tag{12}$$

where $v_{1p}=F_{\text{pre}}/EI^{1/2}$ is the ratio of the preload force to the stiffness, and $v_2=r_0/I^{1/4}$ is the ratio of the initial radius to the moment of inertia. Figure 4 shows the FEM deduced relation between the maximum strain S and the preload force ratio v_{1p} for different initial radius ratios v_2.

When no preload force is applied to the spring ($v_{1p}=0$), the initial strain, being uniformly and constantly distributed, is inversely proportional to the initial radius of the half round spring. For the same initial radius v_2, an increase of the preload force v_{1p} causes a rise in the maximum strain S. When the radius ratio $v_2<70$, the maximum strain S is in linear relation to the preload force v_{1p}, and the $S-v_{1p}$ curves are almost parallel to each other. For $v_2>70$, the $S-v_{1p}$ curves have a larger slope; in other words, the preload force has larger influence on the maximum strain. When the preload force ratio v_{1p} increases, $S-v_{1p}$ curves tend to approach an asymptotic line. This asymptote is the $S-v_{1p}$ curve by $v_2=\infty$. Under large preload conditions, the influence of the initial radius on the maximum strain is less obvious. Therefore it is inefficient to minimize the initial strain by enlarging the initial radius of the spring.

The guiding direction and the preload direction are set perpendicular to each other. And the stiffness in the preload direction determines the maximum loading capability of the spring. To analyze the sensitivity of the stiffness, the five main influential parameters—F_{pre}, r_0, E, I, δ—are converted into the dimensionless Eq. (13),

$$v_{1p}=\frac{F_{pre}}{EI^{1/2}}=f\left(\frac{r_0}{I^{1/4}},\frac{\delta}{r_0}\right)=f(v_2,v_3), \tag{13}$$

where $v_3=\delta/r_0$ is the ratio of the preload displacement to the initial radius. Figure 5 shows the relation between the preload displacement v_3 and the preload force v_{1p} deduced from FEM results for different initial radius ratios v_2.

The stiffness in the preload direction is defined by the slope of the $v_{1p}-v_3$ curve, and its value is obtained at the operating point of the slope. When the initial radius ratio $v_2<70$, the $v_{1p}-v_3$ curves remains linear. For $v_2>70$, the $v_{1p}-v_3$ curve turns from linear into nonlinear, and the slope becomes larger. By applying curve fitting method in the linear range of the curve, the stiffness of the belt-shaped spring in preload direction $k_{lin}=2.5228\,EI/r_0^3$, and the average value of R^2 of the regression curves 0.987 can be deduced.

The belt-shaped spring generates a reaction force in the guiding direction, which is defined as the recovery force F_a and is influenced by the guided displacement X_a. Equation (14) describes the dependence of the maximum stress $\sigma_{\max}$ on the initial and preload conditions, and the guided displacement. Equation (15) shows the relation between the recovery force and the guided displacement for different initial and preload conditions. The ratio of the axial guided displacement to the initial radius is $v_4=X_a/r_0$, and $v_{1a}=F_a/EI^{1/2}$ represents the ratio of the recovery force to the stiffness,

$$S=\frac{\sigma_{\max}}{E}=f_3\left(\frac{r_0}{I^{1/4}},\frac{\delta}{r_0},\frac{x_a}{r_0}\right)=f_3(v_2,v_3,v_4), \tag{14}$$

$$v_{1a}=\frac{F_a}{EI^{1/2}}=f_3\left(\frac{r_0}{I^{1/4}},\frac{\delta}{r_0},\frac{x_a}{r_0}\right)=f_3(v_2,v_3,v_4). \tag{15}$$

By a preload displacement ratios $v_3=0.6$, the relation between the recovery force ratio v_{1a} and the guided displacement ratio v_4 for different initial radius ratios v_2 is shown in Fig. 6. The guided displacement with a constant recovery force is defined by x_{equ},

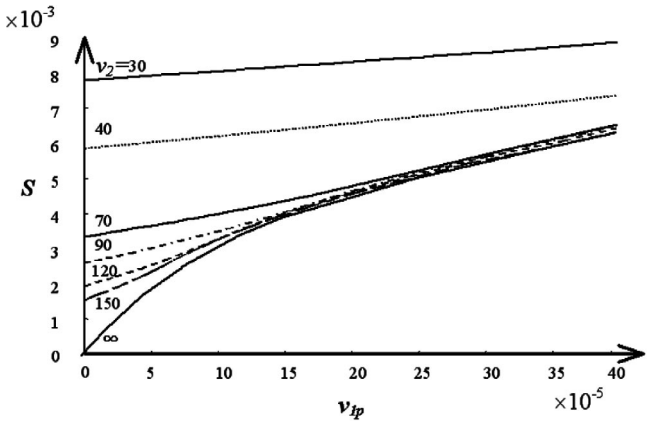

Fig. 4 Maximum strain S versus preload force ratio v_{1p} for different initial radius ratios v_2 ($S-v_{1p}$ curves)

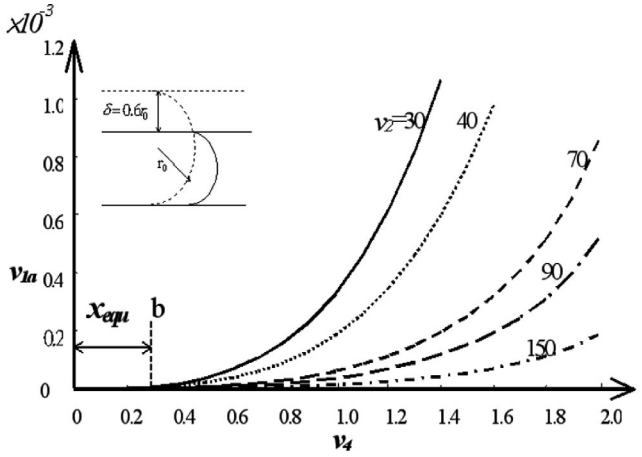

Fig. 6 Recovery force ratio v_{1a} versus guided displacement ratio v_4 for different initial radius ratios v_2, ($v_{1a}-v_4$ curves), preload displacement ratios $v_3=0.6$

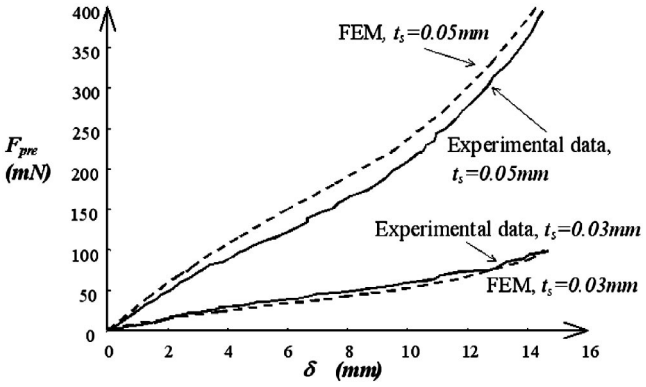

Fig. 8 Preload force F_{pre} as a function of preload displacement δ

whose recovery force is almost zero, which means a nearly frictionless guiding function with a very small reaction force. And the value of x_{equ} can be extended by increasing the preload displacement δ.

Given a preload displacement ratio $v_3=0.6$, the dependences between the maximum strain S and the guided displacement ratio v_4 for different initial radius ratios v_2 are shown in Fig. 7. The maximum stress σ_{max} is inversely proportional to the initial radius r_0. On the $S-v_4$ curves, there exists a range with constant maximum strain and recovery force. Beyond the range with constant recovery force, the spring creates more recovery force, yet maintains its maximum strain. The elastic energy redistributes gradually from the maximum strain in the central bending zone to the entire spring, and causes an increase of the average strain level.

3 Experimental Investigations

Normally, the properties of the spring guide are mainly determined by the preload displacement. Figure 8 shows the relation between the preload force F_{pre} and the preload displacement δ of the 12.7-mm-wide steel sheets with an initial radius of 14 mm. Both of the curves have good linearity; the 0.03-mm and 0.05-mm-thick springs have each a stiffness of 5.29 and 26.57 mN/mm, respectively. The figure shows that a thicker spring can create larger stiffness in the preload direction and consequently increase the load capacity. The experiments demonstrate relatively similar results as the analysis, and the deviation can be attributed to the tolerance of the fixing boundary.

Moreover, energy exchanges are found between the bending and the flattening parts of the belt-shaped spring as the spring rolls. Ideally, the belt-shaped spring could roll with very tiny force. An experimental setup for measuring the relation between reaction force and displacement is shown in Fig. 9. A linear variable-differential transformer (LVDT) sensor is used to measure the guided displacement, and a load cell to measure the reaction force. Two precision stages are applied for adjusting the preload displacement, and another stage for controlling the clamping angle. Figure 10 shows the relation between the recovery force F_a and the guided displacement X_a of two 12.7-mm-wide steel sheets with an initial radius of 12.5 mm (length $=25\pi$ mm). These steel sheets are preloaded with the same preload displacement of 8.85 mm. The guided displacement of the 0.03-mm-thick spring can reach 6 mm with a constant recovery force, while that of the 0.05-mm-thick spring can reach up to 9 mm. Because the real spring boundary is different from the ideal

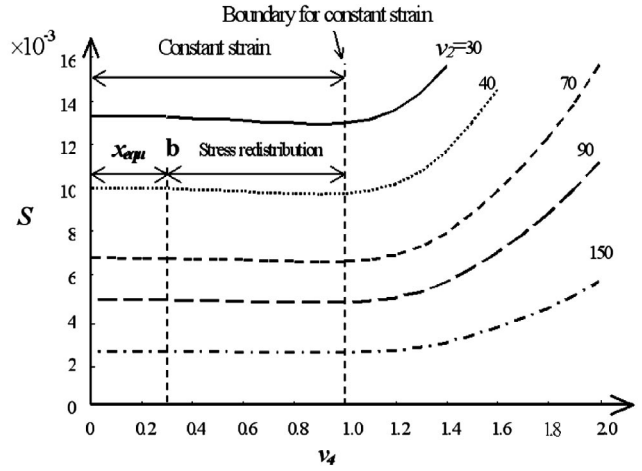

Fig. 7 Maximum strain S versus guided displacement ratio v_4 for different radius ratios v_2 ($S-v_4$ curves), preload displacement ratio $v_3=0.6$

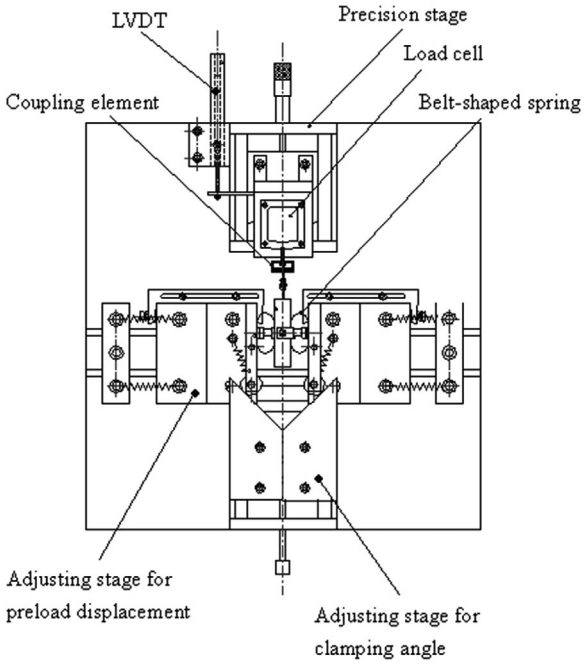

Fig. 9 Experimental setup

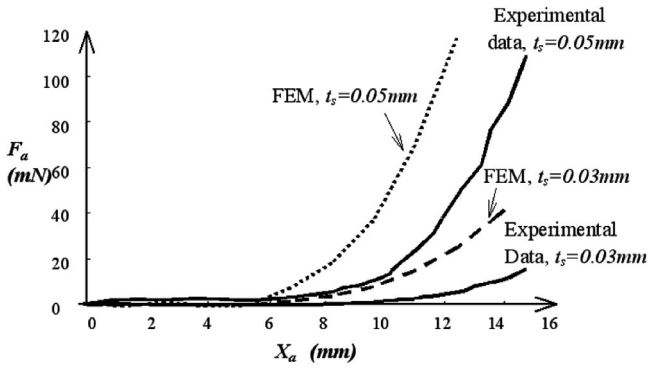

Fig. 10 Recovery force F_a versus guided displacement X_a

rigid boundary defined in FEM analyses, the experimental results are smaller than the FEM analytical results beyond the guided displacement with a constant recovery force.

When the belt-shaped spring is unsymmetrically preloaded, the spring changes its balance position sidewards. Figure 11 shows the relation between the recovery force F_a and the guided displacement X_a for different clamping angles θ_a. The recovery force grows with the increase of the clamping angle. Moreover, the recovery force constant C_θ (=3.43 mN/deg) deduced is dependent on the the clamping angle θ_a, and is determined by the moment of inertia, the initial radius, and the preload displacement. Therefore the spring guide can also be applied to generate specific constant force over a large guided displacement by a linear adjustment of the clamping angle.

4 Guiding Error Analysis

During the guided displacement, the stress distributions of the spring change, which makes the supporting boundaries change their stiffnesses. This unsymmetrical loading causes the guided element to lose its balance. From the FEM analytical results, the preloaded belt-shaped spring can be simplified with two equivalent springs as shown in Fig. 12(a). The acting points of the equivalent springs are located at the positions with the maximum contact pressures, and possess both functions of guiding and supporting. The guided displacement shifts the center of gravity of the guided element out of the symmetric center of two equivalent springs, and these springs thus have different deformations δ_1 and δ_2 as shown in Fig. 12(b).

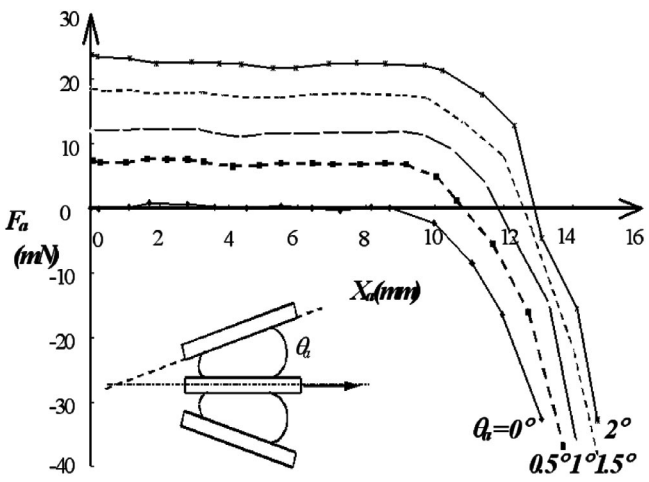

Fig. 11 Recovery force F_a versus clamping angle θ_a

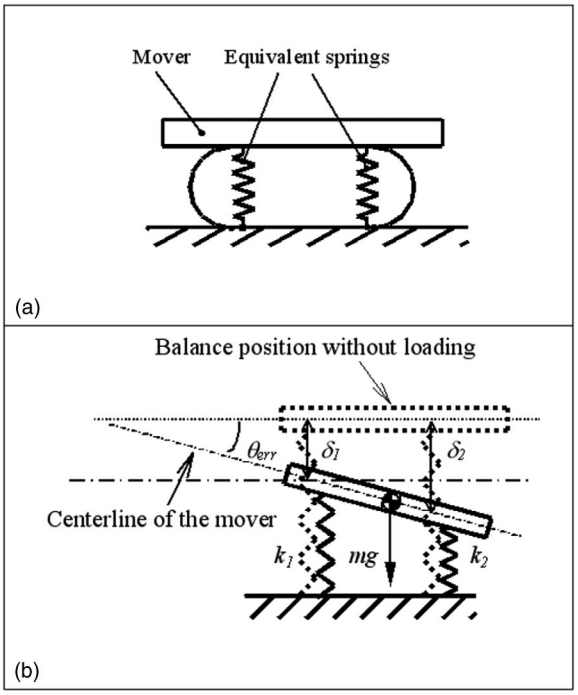

Fig. 12 (*a*) Equivalent springs and (*b*) relation between pitching angle and unbalanced loading

Figure 13 shows the pitching angle error θ_{err} deduced from the geometric relationship in the free body diagram, and a_0 is the initial gravity center, and L is the distance between two equivalent springs. Both equivalent springs each have spring constant k_1 and k_2, and the same initial preloaded deformation δ_0. When the spring guiding system is moved by a displacement X_a, both equivalent springs have their deformations δ_1 and δ_2, respectively, as shown in Eqs. (16) and (17). Therefore from the different deformations of the springs, the pitching angle error θ_{err} can be derived as shown in Eq. (18), where m is the mass of the guided element, and k_{pre} is the initial stiffness of each preloaded spring. Because the parameters in Eq. (18) are not independent, the solution of θ_{err} is then nonlinearly relative to other parameters,

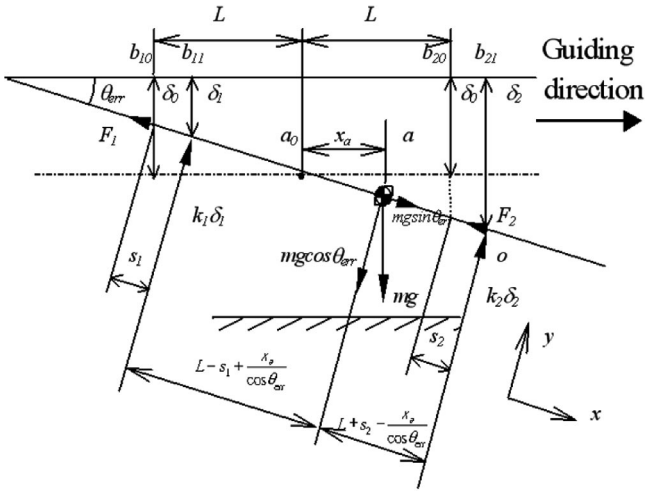

Fig. 13 Free body diagram in a pitched situation

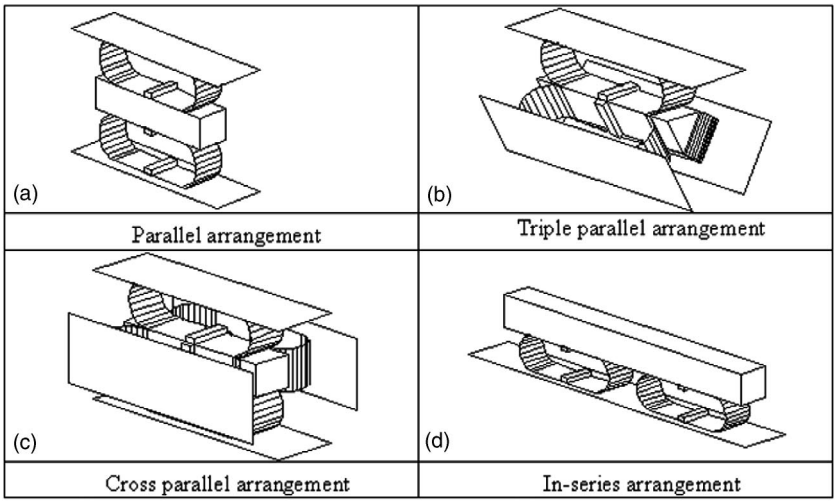

Fig. 14 Design variations for long-stroke guiding system

$$\delta_1 = \left(\frac{L + \frac{\pi}{8}\frac{mg}{k_{\text{pre}}} - \frac{x_a}{\cos\theta_{\text{err}}}}{2k_1 L + \frac{\pi}{4} mg\cos\theta_{\text{err}}} \right) \cdot mg\cos\theta_{\text{err}}, \tag{16}$$

$$\delta_2 = \left(\frac{\frac{k_1}{k_2}L + \frac{\pi}{8}\frac{mg}{k_{\text{pre}}}\left(\frac{2k_{\text{pre}}\cos\theta_{\text{err}}}{k_2} - \frac{k_1}{k_2}\right) + \frac{x_a}{\cos\theta_{\text{err}}}\frac{k_1}{k_2}}{2k_1 L + \frac{\pi}{4} mg\cos\theta_{\text{err}}} \right) \cdot mg\cos\theta_{\text{err}}, \tag{17}$$

$$\sin\theta_{\text{err}} = \frac{\delta_2 - \delta_1}{2L} = \left(\frac{L\left(\frac{k_1}{k_2} - 1\right) + \frac{\pi}{8}\frac{mg}{k_{\text{pre}}}\left(\frac{2k_{\text{pre}}\cos\theta_{\text{err}}}{k_2} - \frac{k_1}{k_2} - 1\right) + \frac{x_a}{\cos\theta_{\text{err}}}\left(\frac{k_1}{k_2} + 1\right)}{2k_{\text{pre}} L + \frac{\pi}{4} mg\cos\theta_{\text{err}}} \right) \frac{mg\cos\theta_{\text{err}}}{2L}. \tag{18}$$

By using an assumption of a small pitching angle error θ_{err}, we can make $k_1 \approx k_2 = k_{\text{pre}}$. Consequently, Eqs. (16)–(18) are transformed into Eqs. (19)–(21):

$$\delta_1 = \left(\frac{1}{2k_{\text{pre}}} - \frac{\frac{\pi}{8}\cdot\frac{mg}{k_{\text{pre}}}(\cos\theta_{\text{err}} - 1) + \frac{x_a}{\cos\theta_{\text{err}}}}{2k_{\text{pre}} L + \frac{\pi}{4} mg\cos\theta_{\text{err}}} \right) \cdot mg\cos\theta_{\text{err}}, \tag{19}$$

$$\delta_2 = \left(\frac{1}{2k_{\text{pre}}} + \frac{\frac{\pi}{8}\cdot\frac{mg}{k_{\text{pre}}}(\cos\theta_{\text{err}} - 1) + \frac{x_a}{\cos\theta_{\text{err}}}}{2k_{\text{pre}} L + \frac{\pi}{4} mg\cos\theta_{\text{err}}} \right) \cdot mg\cos\theta_{err}, \tag{20}$$

$$\sin\theta_{err} = \left(\frac{\frac{\pi}{8}\cdot\frac{mg}{k_{\text{pre}}}(\cos\theta_{\text{err}} - 1) + \frac{x_a}{\cos\theta_{\text{err}}}}{2k_{\text{pre}} L + \frac{\pi}{4} mg\cos\theta_{\text{err}}} \right) \frac{mg\cos\theta_{\text{err}}}{L}. \tag{21}$$

Equations (22)–(25) are deduced through the linearization process with a small θ_{err},

$$\sin\theta_{\text{err}} \approx \theta_{\text{err}}, \tag{22}$$

$$\cos^2\theta_{\text{err}} \approx 1 - \theta_{\text{err}}^2 \approx 1; \tag{23}$$

$$\cos\theta_{\text{err}} \approx 1 - \frac{1}{2}\theta_{\text{err}}^2 \approx 1; \tag{24}$$

$$\sin\theta_{\text{err}}\cos\theta_{\text{err}} \approx \theta_{\text{err}} + \frac{2}{3}\theta_{\text{err}}^3 \approx \theta_{\text{err}}. \tag{25}$$

Then, the Eq. (21) is simplified into Eq. (26):

$$\left(-\frac{\pi}{6}mgL\right)\theta_{\text{err}}^3 - \left[\frac{\pi}{16}\frac{(mg)^2}{k_{\text{pre}}}\right]\theta_{\text{err}}^2 - \left(2k_{\text{pre}}L^2 + \frac{\pi}{4}mgL\right)\theta_{\text{err}} + mgx_a = 0. \tag{26}$$

Since θ_{err}^2 and θ_{err}^3 are very small, the linear relation between the pitching angle error θ_{err} and the guided displacement X_a shown in Eq. (27) can be derived from Eq. (26):

$$\theta_{err} = \frac{mg\cdot x_a}{2k_{pre}\cdot L^2 + \frac{\pi}{4}mg\cdot L}. \tag{27}$$

Based on the Eq. (27), we can minimize the pitching angle error through varying the design parameters. There are four design alternatives for improving the guiding quality shown in Fig. 14. When the springs act in parallel, the number of springs n_s has a positive influence on the pitching angle error as shown in

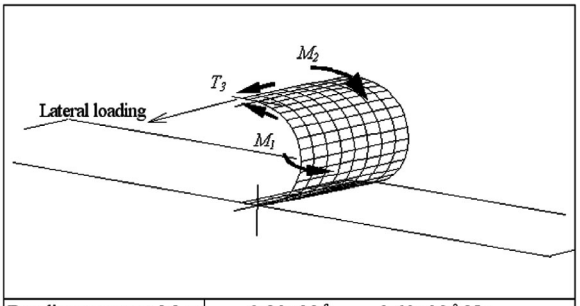

Bending moment M_1 =	2.81×10^{-3} - 1.63×10^{-2} Nm
Bending moment M_2 =	6.49×10^{-3} - 3.29×10^{-1} Nm
Torque T_3 =	-1.79×10^{-2} - 5.51×10^{-2} Nm
Steel spring 50 mm×35.7 mm×0.05 mm (L×W×T)	
Initial radius r_0 = 14 mm	
Young's Modulus $E=190\times10^3$ N/mm^2	
Lateral displacement: 3 mm	

Fig. 15 Analytical model and moments for a lateral loading

Eq. (28). In the series arrangement of springs shown in Fig. 14(*d*) increases the supporting positions and the supporting distance L,

$$\theta_{\text{err}}=\frac{mg\cdot x_a}{2n_s\cdot k_{\text{pre}}\cdot L^2+\frac{\pi}{4}mg\cdot L}. \tag{28}$$

As shown in Eq. (29), the pitching angle error θ_{err} induces a recovery force F_a, which acts against the unbalance force $mg\sin\theta_{\text{err}}$, and the stiffness C_θ here is derived from Fig. 11,

$$F_a=\frac{C_\theta\cdot\theta_{err}}{2}=\left(\frac{mg\cdot x_a}{4k_{pre}\cdot L^2+\frac{\pi}{2}mg\cdot L}\right)C_\theta. \tag{29}$$

For applications in different orientations, the lateral stiffness of the spring guiding system can be improved through geometrical optimization or arrangement of springs along the lateral direction. By a lateral displacement of 3 mm, the bending moments M_1, M_2, and torque T_3 are shown in Fig. 15. With no lateral displacement, only the bending moment M_2 can be given. A lateral displacement generates a new bending moment M_1 and a torque T_3, while the existing moment M_2 also increases larger than the other moments. Besides, the maximum of M_2 occurs on the opposite side of the lateral displacement. In consideration of the smooth guiding and the maximum stress, the lateral stiffness can be efficiently improved through increasing the torsional stiffness over the 1-2 plane. Figure 16 shows the design idea of improving the lateral stiffness by using the cross-shaped groove pattern on the spring. For an optimal result, the pattern angle θ_s can be variable over the spring surface.

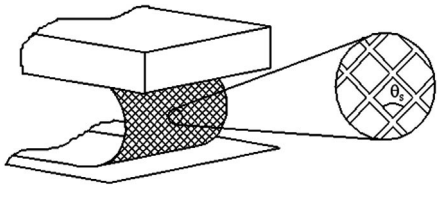

Fig. 16 Cross-shaped groove pattern on spring surface for improving lateral stiffness

5 Conclusion

The long-stroke spring guiding system developed in this study utilizes preloaded belt-shaped spring to realize the guiding function through rolling movement. The mechanical energy recovered from spring flattening is transferred directly back to the work for spring bending. The recovery force (i.e., the reaction force) of the spring guide is negligibly small, and only the phenomenon of molecular friction in the spring to be overcome. Moreover, through variation of the clamping angle the recovery force can be regulated, and which generates a constant force for large displacement. The guided stroke is dependent on the spring length and the preload displacement, and can even reach millimeter range. The monolithic flexure device used in micro-positioners has a guided stroke of about 1/100 spring size, and the belt-shaped long-stroke spring guiding system developed here can achieve a maximum guided stroke up to 0.16 of the total spring length. The larger the preload displacement is applied, the larger the maximum stress and strain can be given. To pursue the highest endurance limit, spring materials with high ratio of the yield strength to the Young's modulus are preferred for the preloaded springs. The pitching angle error can either be minimized through parallel arrangement of springs or by lowering of gravity center. For an efficient design of the spring guiding system, the FEM analytical results are transformed into dimensionless relationships by using the Buckingham pi theorem. These dimensionless relationships are then combined with the design boundary conditions to derive the governing equations and the design evaluation. Simple form and great variability make the long-stroke spring guiding system relatively adaptable to different applications in precision systems and microsystems.

References

[1] Slocum, A. H., 1992, *Precision Machine Design*, Prentice-Hall International Editions, Singapore, pp. 521–538.

[2] Bosch, D., Heimhofer, B., Mück, G., Seidel, H., Thumser, U., and Welser, W., 1993, "A Silicon Microvalve with Combined Electromagnetic/Electrostatic Actuation," Sens. Actuators, A, **37–38**, pp. 684–692.

[3] Elwenspoek, M., Smith, L., and Hök, B., 1991, "Active Joints for Microrobot Limbs," J. Micromech. Microeng., **2**, pp. 221–223.

[4] Trimmer, W. S. N., 1989, "Microrobots and Micromechanical Systems," Sens. Actuators, **19**, pp. 267–287.

[5] Uenishi, Y., Tsugai, M., and Mehregany, M., 1995, "Micro-Opto-Mechanical Devices Fabricated by Anisotropic Etching of (110) Silicon," J. Micromech. Microeng., **5**, pp. 305–312.

[6] Portman, V., and Sandler, B. Z., 1999, "High-Stiffness Precision Actuator for Small Displacements," Int. J. Mach. Tools Manuf., **39**, pp. 823–837.

[7] Park, K. H., Choi, C. H., and Ryu, J., 2001, "Hybrid Actuator for High Speed and High Precision Optical Disk Drives," Mechatronics, **11**, pp. 527–543.

[8] Lutwyche, M. I., and Wada, Y., 1995, "Manufacture of Micromechanical Scanning Tunneling Microscopes for Observation of the Tip Apex in a Transmission Electron Microscope," Sens. Actuators, A, **48**, pp. 127–136.

[9] Billing, V., 1960, "Flexures," Mach. Des., pp. 114–119.

[10] Smith, S. T., Chetwynd, D. G., and Bowen, D. K., 1987, "Design and Assessment of Monolithic High Translation Mechanism," J. Phys. E, **20**, pp. 977–987.

[11] Narayansamy, K., and Srinivasa, Y. G., 2000, *Precision Engineering*, Narosa Publishing House, New Delhi, pp. 421–428.

[12] Lobontiu, N., and Paine, J. S. N., 2002, "Design of Circular Cross-Section Corner-Filleted Flexure Hinges for Three Dimensional Compliant Mechanisms," J. Mech. Des., **124**, pp. 479–484.

[13] Demus, W., Linearverstellvorrichtung, Max-Plank-Gesellschaft e.V., DE-Patentanmeldung P 3343 340 C1, München, Nov. 1983.

[14] Buckingham, E., 1914, "On Physically Similar Systems; Illustrations of the Use of Dimensional Equations," Phys. Rev., **4**, pp. 345–376.

[15] Vanderplaats, Garret N., 1993, *Numerical Optimization Techniques for Engineering Design*, McGraw-Hill International Editions, Singapore.